Journal of The Electrochemical Society

ACCEPTED MANUSCRIPT • OPEN ACCESS

Coupling of 3D Porous Hosts for Li Metal Battery Anodes with Viscous Polymer Electrolytes

To cite this article before publication: Bumjun Park *et al* 2022 *J. Electrochem. Soc.* in press https://doi.org/10.1149/1945-7111/ac47ea

Coupling of 3D Porous Hosts for Li Metal Battery Anodes with Viscous Polymer Electrolytes

Journal:	*Journal of The Electrochemical Society*
Manuscript ID	JES-106174.R2
Manuscript Type:	Research Paper
Date Submitted by the Author:	17-Dec-2021
Complete List of Authors:	Park, Bumjun; University of Notre Dame, Department of Chemical & Biomolecular Engineering Oh, Christiana; University of Notre Dame Yu, Sooyoun; University of Notre Dame Yang, Bingxin ; University of Notre Dame Myung, Nosang; University of California, Riverside, Chemical and Environmental Engineering Bohn, Paul; University of Notre Dame Schaefer, Jennifer; University of Notre Dame, Department of Chemical & Biomolecular Engineering
Keywords:	Batteries - Lithium, Electrodeposition, Energy Storage

Coupling of 3D Porous Hosts for Li Metal Battery Anodes with Viscous Polymer Electrolytes

Bumjun Park,[1,*] Christiana Oh,[1,**] Sooyoun Yu,[1,**] Bingxin Yang,[1] Nosang V. Myung,[1,**] Paul W. Bohn,[1,2] and Jennifer L. Schaefer[1,**,z]

[1] Department of Chemical and Biomolecular Engineering, University of Notre Dame, Notre Dame, Indiana 46556, United States

[2] Department of Chemistry and Biochemistry, University of Notre Dame, Notre Dame, Indiana 46556, United States

*Electrochemical Society Student Member.

**Electrochemical Society Member.

[z]E-mail: Jennifer.L.Schaefer.43@nd.edu

Abstract

As the energy storage markets demand increased capacity of rechargeable batteries, Li metal anodes have regained major attention due to their high theoretical specific capacity. However, Li anodes tend to have dendritic growth and constant electrolyte consumption upon cycling, which lead to safety concerns, low Coulombic efficiency, and short cycle life of the battery. In this work, both conductive and non-conductive 3D porous hosts were coupled with a viscous (melt) polymer electrolyte. The cross-section of the hosts showed good contact between porous hosts and the melt polymer electrolyte before and after extensive cycling, indicating that the viscous electrolyte successfully refilled the space upon Li stripping. Upon deep Li deposition/stripping cycling (5 mAh cm^{-2}), the non-conductive host with the viscous electrolyte successfully cycled,

while conductive host allowed rapid short circuiting. Post-mortem cross-sectional imaging showed that the Li deposition was confined to the top layers of the host. COMSOL simulations indicated that current density was higher and more restricted to the top of the conductive host with the polymer electrolyte than the liquid electrolyte. This resulted in quicker short circuiting of the polymer electrolyte cell during deep cycling. Thus, the non-conductive 3D host is preferred for coupling with the melt polymer electrolyte.

This paper 97, was presented during the 240th Meeting of the Electrochemical Society, October 10 – 14, 2021.

1. Introduction

In efforts to resolve environmental issues caused by fossil fuels such as global warming and air pollution, there is widespread global effort to develop renewable energy sources, electric vehicles (EVs), and electric public transportation.[1,2] Rechargeable batteries play a key role in such devices and are required to deliver higher energy density to enable aerial vehicles and longer range heavy duty trucks. In order to overcome the intrinsic energy density limit with commercial LIBs, next generation "beyond Li-ion" battery technologies have been investigated.[4–14] Li metal has regained attention as an anode for next generation batteries due to its high gravimetric charge capacity (3862 mAh g^{-1}) compared with graphite anodes (372 mAh g^{-1}).[15]

However, Li dendritic growth and constant electrolyte consumption upon repeated cycling cause safety issues, low Coulombic efficiency and life cycle performance issues.[16,17] Such drawbacks have been obstacles for the commercialization of Li metal as anodes for decades.[18] There have been studies to address those problems by improving electrolytes or the Li-electrolyte interface, such as electrolyte additives,[19–23] artificial solid electrolyte interphase (SEI)

and coatings,[24–26] single Li^+ ion conductors,[27–30] and solid-state electrolytes.[31,32] This strategy attempts to stabilize Li^+ deposition by protecting the interface and homogenizing Li^+ transport onto the electrode surface. In the meantime, 3D porous host materials for Li metal anodes have been studied as another strategy, including conductive 3D hosts such as surface modified Li metal,[33] Cu substrates,[34–36] ZnO-coated polyimide nanofibers,[37] Si-coated porous carbon,[38] reduced graphene oxides,[39,40] as well as non-conductive 3D hosts such as polyacrylonitrile (PAN) nanofibers[41] and functionalized glass fibers.[42] This strategy attempts to stabilize Li deposition by accommodating the Li deposition within the structure, whereas pore sizes of similar or smaller size than the typical Li dendrite diameter allow for uniform rather than dendritic deposition.

At the same time, more thermally and mechanically stable electrolytes are sought to increase safety. While the reports on 3D hosts suggest that porous electrode hosts effectively accommodate Li growth within the host structure, inclusion of flammable liquid electrolytes can result in safety issues such as flammability and leakage of the electrolyte. Solid polymer electrolytes are thermally and mechanically more stable than liquid electrolytes and thus may reduce the safety issues. However, a suitable electrolyte for pairing with a 3D porous host must fill the host pore volume. Here we report 3D porous electrode hosts coupled with a viscous (melt) polymer electrolyte to minimize issues from Li metal anodes. ZnO filler were added to increase lithiophilicity of the mats, to facilitate Li growth within the mats more effectively. The melt polymer electrolyte is expected to maintain good contact with porous hosts and accommodate Li deposit during Li deposition/stripping cycling. Both conductive (Cu nanowires)[34] and non-conductive (electrospun PAN nanofiber)[41] 3D porous hosts were tested with the viscous polymer electrolyte and compared with the liquid electrolyte. Both types of 3D

porous hosts successfully cycled without short circuiting during one cycle of extensive Li deposition/stripping cycling (5 mAh cm^{-2}) with the liquid electrolyte. However, while the cell with the non-conductive host with the melt polymer electrolyte was cycled without short circuiting during one deep cycle, the cell with the conductive host was quickly short circuited. COMSOL simulation results indicated that the current density was mostly concentrated on the top layers of the conductive host, while the current density was uniform with the non-conductive host with both melt polymer and liquid electrolytes. Specifically, the current density was more severely concentrated on the first layer with the viscous polymer electrolyte, which resulted in the major Li deposition on the top of the conductive host and eventually short circuited quickly.

2. Experimental

2.1.Materials

Lithium bis(trifluoromethanesulfonyl)imide (LiTFSI, TCI) was dried at 120 ºC for 12 h under vacuum. Poly(ethylene glycol) dimethyl ether (PEGDME, M_n = 1000 g mol^{-1}) was dried under vacuum for 72 h. Liquid electrolyte solvents, 1,2-dimethoxyethane (DME, Sigma) and 1,3-dioxolane (DOL, Sigma) were dried with molecular sieves (Sigma, 3 Å) for 48 h. Abovementioned treatments were conducted in an argon-filled glovebox.

Tetrabutylammonium bromide (TBAB, Sigma), dimethylformamide (DMF, Sigma), hexamethylenetetramine (HMTA, Sigma), zinc nitrate ($Zn(NO_3)_2$, Sigma), sodium hydroxide (NaOH, Sigma), copper nitrate ($Cu(NO_3)_2$, Sigma), ethylenediamine (Sigma), hydrazine (35 wt.% in water, Sigma) were used as received.

2.2.Preparation of a non-conductive porous host matrix (PAN-ZnO)

Poly(acrylonitrile) (PAN, 0.821 g), ZnO nanoparticles (1.524 g), and TBAB (0.119 g) were added to DMF (10 mL) and stirred for overnight. The solution was then electrospun (15 kV, 20 gauge syringe, 23 ºC, 60% RH humidity, 15 cm distance, Al foil collector) to form a PAN-ZnO nanofiber mat with white color (**Figure S1a**).[43]

Hydrothermal growth of ZnO was then performed on the previously obtained nanofiber mat by a previously reported method.[44] Electrospun PAN-ZnO nanofiber mats were held together with a Cu sheet. The two layers were cut together into smaller pieces, during which the pressure of the scissors laminated the two layers together at the edges. The segments of the nanofiber mat and Cu sheet were stirred in an aqueous solution of 0.1 M $Zn(NO_3)_2$ and 0.1 M HMTA at room temperature for 24 h. The solution was then heated to 90ºC for 5 h. The resulting nanofiber mat (**Figure S1b**) on copper was washed with DI water and then dried at room temperature overnight. The nanofiber mat on copper was then heated to 280 ºC for 1 h in air to thermally stabilize the PAN to obtain a ZnO-coated PAN-ZnO nanofiber mat (**Figure 1a**). The thermally stabilized PAN-ZnO mat electrodes were used as a non-conductive porous host for the electrochemical measurements.

2.3.*Preparation of a conductive porous host matrix (Cu-ZnO)*

Cu nanowires were prepared by a previously reported method.[34,45] In brief, $Cu(NO_3)_2$, ethylenediamine, and hydrazine were added, in the order mentioned, into 15 M NaOH solution in a round bottom flask under nitrogen atmosphere. The solution was stirred for 5 min after each addition of reagents for uniform mixing. The total solution was stirred at 80ºC and 200 rpm for 1 h. The Cu nanowires were suspended on the solution interface and the solution on the bottom

was decanted. The Cu nanowires were then washed with DI water, centrifuged at 6000 rpm for 5 min, and then the supernatant was decanted. This process was repeated three times. Finally, the Cu nanowires were washed in ethanol three times. The Cu nanowires were stored in a mixture of ethanol and 3 wt.% hydrazine solution (5/1, v/v). The concentration of the Cu nanowire was ~22.5 mg mL^{-1}.

To prepare Cu-ZnO mat electrodes, ZnO nanoparticles (0.165 g) were added to the Cu nanowire solution (14.6 mL) and sonicated for 5 min. The solution was then cast on stainless steel disks at room temperature overnight. The cast Cu-ZnO mats were annealed at 450 ºC for 4 h under the H_2/Ar (5%/95%) flow. The annealed Cu-ZnO mat electrodes were used as a conductive porous host for electrochemical tests (**Figure 1c**).

2.4.Scanning electron microscopy (SEM)

Morphologies of synthesized porous hosts were investigated with a FEI Magellan 400 at an accelerating voltage of 5 kV and current of 13 pA at a working distance of 4 mm. Post-mortem samples were sealed in a Pelco SEM pin stub vacuum desiccator in an argon-filled glovebox and then transferred to the instrument to minimize air exposure. Post-mortem, cross-sectional SEM images of Cu-ZnO or PPN-ZnO electrodes were also obtained after deep cycling. Electrodes after deposition and after deposition/stripping were compared to see reversible deposition/stripping of Li. For the cross-section images, post-mortem samples were fractured in liquid nitrogen.

2.5. Ionic conductivity

Ionic conductivity was measured by using a broadband dielectric spectrometer with an Alpha A analyzer, outfitted with a cryostat and Quatro temperature control unit (Novocontrol Technologies). Samples were placed between two stainless steel (SS) electrodes with glass fiber spacers with a thickness of 53 μm. Dielectric spectroscopy was measured over a frequency range of 10^7 - 10^{-1} Hz with an amplitude of 0.5 V over a temperature range from -30 to 100 °C in 5 °C intervals. Temperature was stabilized at each point for 10 min within 0.5 °C before measurement. The ionic conductivity of LiTFSI in PEGDME (EO:Li=20:1) at 50 ºC, where the deposition/stripping cycling with the viscous polymer electrolyte was performed, was around 6.54×10^{-4} S cm^{-1}. 1 M LiTFSI in DOL/DME showed ionic conductivity of 2.53×10^{-3} S cm^{-1} at 25 ºC (**Figure S2**).

2.6. Coin cell battery test

In order to perform electrochemical tests, CR2032 coin cells were assembled using cell components as described as follows. A porous host matrix (Cu-ZnO or PAN-ZnO mats) was used as a working electrode for the battery cell tests (Li|Cu-ZnO or Li|PAN-ZnO cells). Here a Li foil was used as a counter electrode and a glass fiber separator was used as a separator. A liquid electrolyte and a viscous polymer electrolyte were prepared as 1.0 M LiTFSI in DOL/DME and LiTFSI in PEGDME (EO:Li=20:1), respectively. Li|Cu-ZnO or Li|PAN-ZnO asymmetric cells were assembled with the two different electrolytes.

Coin cells with the polymer electrolyte were aged at 120 ºC for 20 h prior to a conditioning step. The coin cells then cycled between 0 – 1 V for 3 – 5 cycles at a current density of 0.05 mA cm^{-2} at 50 ºC as a conditioning step (**Figure S3 and Figure S4**). The cells after the conditioning step underwent either a rate capability test or deep cycling test. Coin cells with the

liquid electrolyte were aged at room temperature for 20 h prior to a conditioning step, which underwent the same procedures at room temperature.

Rate capability tests were conducted at different current density (0.1, 0.2, 0.3, 0.5, 1, 2, 5 mA cm^{-2}) with a charge capacity of 1 mAh cm^{-2} for the deposition step and a cutoff voltage of 1 V for the stripping step. Slow rate capability tests were conducted at current density of 0.01, 0.025, 0.05, 0.1, 0.125, 0.15, 0.175, 0.2 mA cm^{-2} with a charge capacity of 0.5 mAh cm^{-2} for the deposition step and a cutoff voltage of 1 V on the stripping step.

Deep cycling tests were conducted at a current density of 0.1 mA cm^{-2} with a charge capacity of 5 mAh cm^{-2} (equivalent to ca. 25 µm thickness of Li metal) and a cutoff voltage of 1 V on the stripping step.

2.7.Electrochemical impedance spectroscopy (EIS)

EIS was performed with a broadband dielectric spectrometer with an Alpha A analyzer (Novocontrol Technologies, Montabaur, Germany). EIS was measured after conditioning, deep deposition, and deep deposition/dissolution with a frequency range of 10^{7} – 10^{-1} Hz with an amplitude of 0.1 V.

2.8.COMSOL simulation

Finite element simulations were performed using COMSOL Multiphysics (Stockholm, Sweden) to simulate Li ion transport and current density distributions in cells with varying electrolyte compositions (liquid and polymer electrolytes). A 2-dimensional domain was developed to represent the cross-sectional geometry and dimensions of the cells (Li metal/Electrolyte/Cu nanowires and substrate). Here, the reaction kinetics associated with Li ion

generation on the Li metal and depletion on the Cu nanowires and substrate surfaces were described by a Butler-Volmer expression for the charge transfer current density i_{loc} (A m^{-2}) given by:

$$i_{loc} = i_o \left(\exp\left(\frac{\alpha_a F \eta}{RT}\right) - \exp\left(\frac{-\alpha_c F \eta}{RT}\right)\right) \quad (1)$$

where i_o is the exchange current density, α_a is the anodic charge transfer coefficient, α_c is the cathodic transfer coefficient, and η is the overpotential.

Cu nanowires were modeled as circular rods (d = 1μm) embedded in the electrolyte structure to elucidate the role of electrode tortuosity on Li ion transport. Simulation results for PAN-ZnO nanowires are detailed in the Supporting Information (SI). The total current on Cu nanowires and the Cu electrode were set to 0.1 mA. For the electrolyte materials, we considered properties such as the Li ion diffusion coefficient, electrolyte conductivity, transport number, and activity coefficient of the liquid and the polymer electrolytes. Further details of the simulations are given in the Supporting Information (SI).

3. Results and Discussion

3.1.SEM of PAN-ZnO and Cu-ZnO (initial)

Figure 1 shows SEM images of PAN-ZnO and Cu-ZnO mats. In both mats, ZnO were used as a lithiophilic additive.[34,37] PAN-ZnO mat (**Figure 1a**) shows fibers with a diameter of ~500 nm with needle-like ZnO on the fiber surface. The Cu-ZnO mat (**Figure 1c**) shows nanowires with a diameter of ~400 nm with uniformly distributed ZnO nanoparticles between Cu nanowires that look like white dots.

In order to check the lithiophilicity of the obtained mat electrodes, the electrodes were put contact with liquid lithium metal at 280 ºC. The color of the matrix became dark gray. The

morphology of both mats (**Figure 1b and 1d**) indicated that the fibers were uniformly covered with Li, implying that the matrices were lithiophilic and the ZnO sites were well connected.

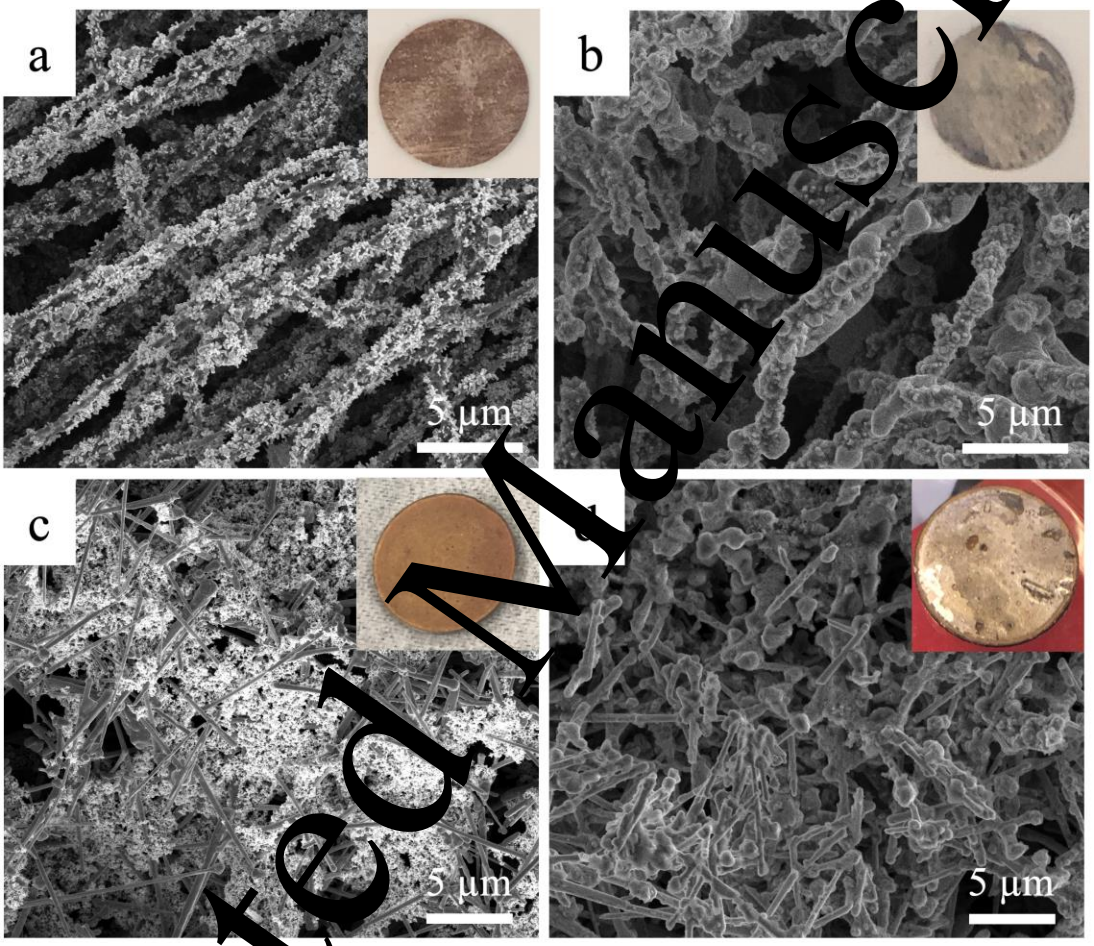

Figure 1. SEM images of PAN-ZnO and Cu-ZnO mats: PAN-ZnO (a) before and (b) after molten Li infusion, Cu-ZnO (c) before and (d) after molten Li infusion.

3.2.Rate capability tests

Li|PAN-ZnO (**Figure 2**) and Li|Cu-ZnO cells (**Figure 3**) with the liquid and polymer electrolytes were cycled 5 times at each current density from 0.1 to 5 mA cm^{-2}. For both Li|PAN-ZnO and Li|Cu-ZnO cells with the liquid and polymer electrolytes, the Coulombic efficiency was similar to the last cycle of the conditioning cycle (~ 80%, **Figure S3a and Figure S4a**) and increased for the first few cycles. This increase of Coulombic efficiency was also observed in the first few cycles (~ 10 cycles) with Li|PAN-ZnO cells at slower rate (**Figure S3c**). This might be due to the irreversible reduction reaction of ZnO and Li-Zn alloy reaction that occurs on newly activated ZnO nanoparticles upon electrical contact.[46,47] Assuming that the Coulombic efficiency loss stems from the loss of Li metal, the loss of Li during the conditioning cycle and the first 5 cycles after the conditioning cycle were ~0.84 mg cm^{-2} (~15.1 µm thickness) and ~0.34 mg cm^{-2} (~6.3 µm thickness) regardless of the cell and electrolyte types. Even though most of the irreversible reaction of Li and ZnO occurs during the conditioning cycling (**Figure S3a and Figure S4a**), especially on the first cycle, where a long plateau at ~0.6 V was observed, it appears that Li deposition proceeds and contacts fresh ZnO surface that did not participate in the irreversible reaction in the previous cycle.

After the first few cycles, the Coulombic efficiency of the liquid electrolyte for both Li|PAN-ZnO cells (**Figure 2c**) and Li|Cu-ZnO cells (**Figure 3c**) reached ~99% and did not decrease within the measured current density. While there was no significant difference in the Coulombic efficiency between Li|PAN-ZnO and Li|Cu-ZnO cells, they showed different voltage vs capacity profiles. Li|PAN-ZnO cell with the liquid electrolyte showed quick voltage drop to ~0 V during the deposition step, where a nucleation peak and following Li deposition plateau was observed (**Figure 2a**). The Li stripping plateau was observed as the stripping step begins and the voltage sharply increased to 1 V at the end of the stripping step. On the other hand, the Li|Cu-

ZnO cell with the liquid electrolyte showed a gentle slope of the voltage over most of the deposition step and reached the Li deposition plateau at the end (**Figure 3a**). Likewise, a gentle increase of the voltage was observed after a short Li stripping plateau. The gentle slope indicates that the Li was reduced to form Li-Zn alloy from ZnO before reaching to the Li deposition overpotential during the deposition step.[46,47] The lack of the gentle slope of the voltage with Li|PAN-ZnO cell is due to the isolation of the ZnO on the PAN nanofibers, unlike Cu-ZnO, where most ZnO was electrically connected to the conductive Cu nanowires. Therefore, it can be inferred that the ZnO in a Li|PAN-ZnO cell will be activated only upon the contact with Li deposit or dendrites that are electrically connected to the substrate. Also, the gap of the applied current and the limiting current might be related to the ratio of active ZnO in the conductive host.

As the applied current density increased in the Li|Cu-ZnO cell with the liquid electrolyte (**Figure 3a**), the voltage reached the Li deposition overpotential earlier (0.7 mAh cm^{-2} at 0.1 mA cm^{-2} to 0.2 mAh cm^{-2} at 5.0 mA cm^{-2}), indicating that the ratio of ZnO that participated in Li-Zn alloy reaction decreased. The Li|Cu-ZnO cell with the polymer electrolyte reached the Li deposition overpotential around 0.1 mAh cm^{-2} at 0.1 mA cm^{-2} (**Figure 3b**). The Coulombic efficiency of Li|Cu-ZnO with the polymer electrolyte (**Figure 3d**) was much lower (~70%) than the liquid electrolyte (**Figure 3c**), implying new irreversible Li-Zn alloy reaction or quick dead Li formation might occur from the low active surface area (or high interfacial resistance). The Coulombic efficiency of Li|Cu-ZnO with the polymer electrolyte did not reach higher than 80% at all tested current densities and was not stable within the same current density. On the other hand, the Coulombic efficiency of the Li|PAN-ZnO cell with the polymer electrolyte showed ~90% at 0.2 mA cm^{-2} and decreased with increased current density, though the Coulombic efficiency was stable within the same current density.

The voltage vs capacity profiles of Li|PAN-ZnO cell with the polymer electrolyte at lower current density (**Figure S5b**) showed gradual increase of the overpotential after the nucleation peak due to the limited diffusion.[48] The deposition overpotential exceeded the nucleation peak above the current density of 0.1 mA cm^{-2}, implying that the applied current density was reaching the limiting current density. On the other hand, with Li|PAN-ZnO with the liquid electrolyte at lower current density (**Figure S5a**), there was a negligible increase of the deposition overpotential with increased current density, while the nucleation peak increased, implying that the applied current density was reasonably lower than the limiting current with no diffusion limitation. The nucleation peak of Li|PAN-ZnO with the liquid and polymer electrolytes were similar (**Figure S5a and Figure S5b**), implying that the nucleation behavior was relatively similar between the liquid and polymer electrolytes.

Since the applied current density of 0.1 mA cm^{-2} to 5.0 mA cm^{-2} might be near or above the limiting current density, both Li|PAN-ZnO and Li|Cu-ZnO cells with the polymer electrolyte showed different voltage vs capacity profiles from the liquid electrolyte. Unlike the liquid electrolyte, significant overpotential (> 1 V) was observed on the deposition step at the current density from 2.0 mA cm^{-2} and 5.0 mA cm^{-2} for Li|PAN-ZnO (**Figure 2b**) and Li|Cu-ZnO (**Figure 3b**) cells, implying that either the Li^+ transport or Li^+ stripping from Li electrode and the deposition on the PAN-ZnO or Cu-ZnO electrodes could not support the applied current density.

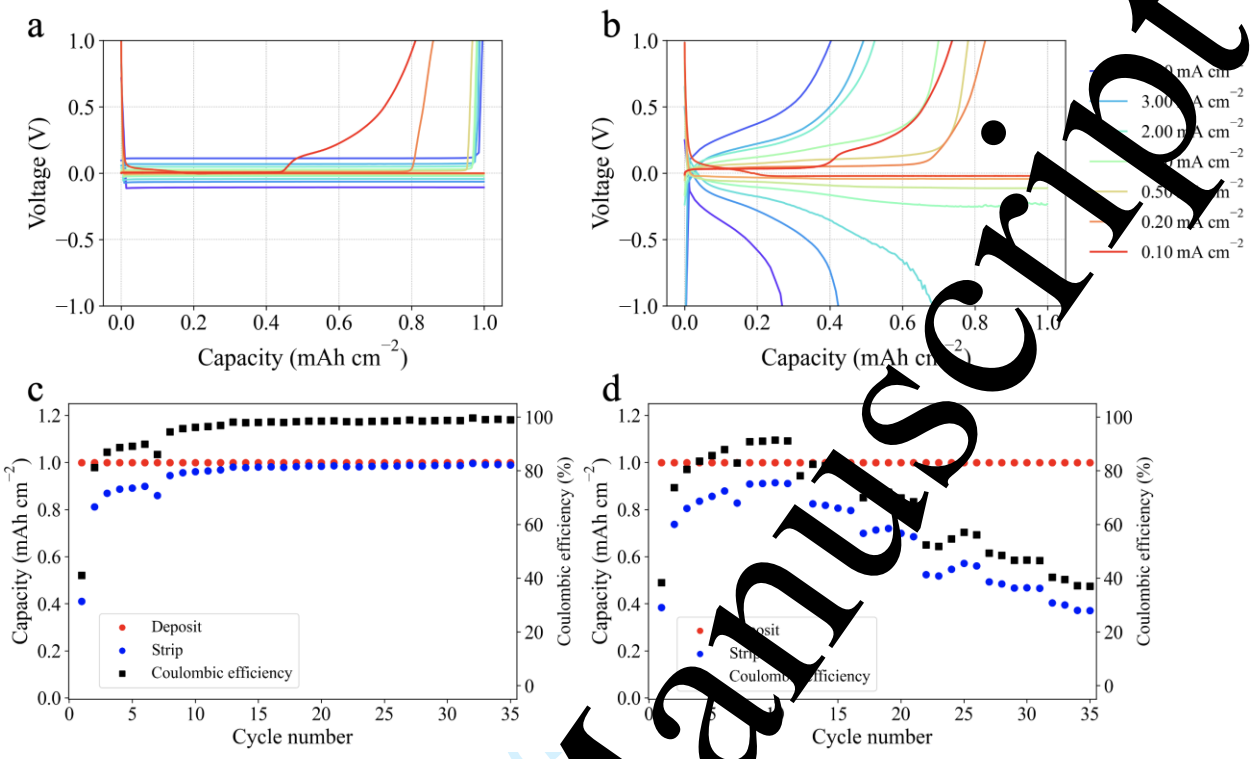

Figure 2. Rate capability of Li|PAN-ZnO cells at different current density (0.1 – 5.0 mA cm^{-2}). Voltage vs capacity curves at each rate with (a) the liquid and (b) polymer electrolytes. Charge and discharge capacity and Coulombic efficiency vs cycle number with (c) the liquid and (d) polymer electrolytes.

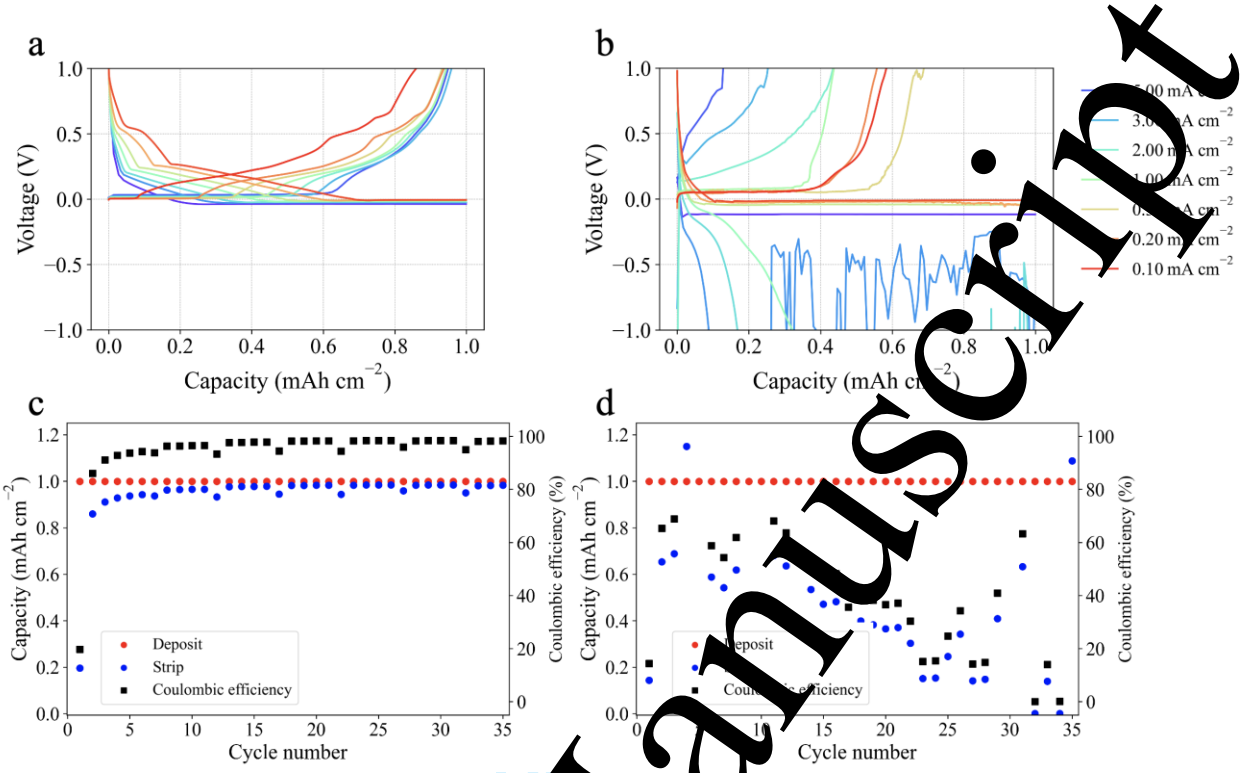

Figure 3. Rate capability of Li|Cu-ZnO cells at different current density (0.1 – 5.0 mA cm^{-2}). Voltage vs capacity curves at each rate with (a) the liquid and (b) polymer electrolytes. Charge and discharge capacity and Coulombic efficiency vs cycle number with (c) the liquid and (d) polymer electrolytes.

3.3.Deep cycling and EIS

Li|PAN-ZnO and Li|Cu-ZnO cells with the liquid and polymer electrolytes after conditioning steps were cycled 5 mAh cm^{-2} at a current density of 0.1 mA cm^{-2}. The voltage vs capacity profiles and the EIS measurements on each step (before deposition, after deposition, and after deposition-stripping) are shown in **Figure 4 and Figure 5**, respectively. There was no significant difference in the Coulombic efficiency (81.8% and 78.5%) and the overpotential (4.3 mV and 4.9 mV) for Li|PAN-ZnO and Li|Cu-ZnO cells with the liquid electrolyte (**Figure 4a and Figure 5a**). The overpotential of Li|PAN-ZnO and Li|Cu-ZnO cells

with the polymer electrolyte were not significantly different (49 mV and 61 mV) (**Figure 5b and Figure 5b**). However, Li|PAN-ZnO cycled successfully with the Coulombic efficiency of 94.5%, while Li|Cu-ZnO cell with the polymer electrolyte was short circuited in either the first stripping (**Figure 5b**) or deposition step (**Figure S6**).

The Coulombic efficiency of Li|PAN-ZnO cells with the polymer electrolyte was about 6% lower than the liquid electrolyte, which might be due to the applied current density being closer to the limiting current of the polymer electrolyte and resulting in more dead Li during cycling. The Coulombic efficiency did not reach 100% for any cells, which results from electrolyte consumption and dead Li formation.

The obtained EIS data (**Figure 4c-d,** and **Figure 5c-d**) were fit to an equivalent circuit model (**Figure S7**). The film resistance (R_{film}) and the charge transfer resistance (R_{ct}) were summed into an interfacial resistance ($R_{int} = R_{film} + R_{ct}$). R_{int} of Li|PAN-ZnO and Li|Cu-ZnO cells before deposition, after deposition, and after stripping are shown in **Figure 4e-f and Figure 5e-f**, respectively.

For both Li|PAN-ZnO and Li|Cu-ZnO cells before deposition, R_{int} was more than 5 times higher with the polymer electrolyte than the liquid electrolyte, even though the polymer electrolyte had a good contact with both PAN-ZnO and Cu-ZnO substrates (**Figure 6 and Figure 7**). While R_{int} of Li|PAN-ZnO (~10 Ω) was slightly higher than Li|Cu-ZnO (~5 Ω) with the liquid electrolyte, the R_{int} of Li|PAN-ZnO (~70 Ω) was lower than Li|Cu-ZnO (~140 Ω) with the polymer electrolyte. It was previously reported that the SEI with low resistance extended the reversible cycling of Li metal.[49] Thus, the higher R_{int} of Li|Cu-ZnO might contribute to the quick short circuit of the cell.

Overall, R_{int} did not change or slightly decreased after deposition except in the case of Cu-ZnO with the polymer electrolyte, which was short circuited during cycling. For Cu-ZnO with the liquid electrolyte and PAN-ZnO with the polymer electrolyte, R_{int} decreased after stripping. R_{int} of PAN-ZnO with the liquid electrolyte increased. However, since R_{film} and R_{ct} for both Cu-ZnO and PAN-ZnO hosts with the polymer electrolyte can not be easily deconvoluted, it is difficult to ascertain if the change in R_{int} was from R_{film} or R_{ct}.

For all types of cells cycled without short circuiting, the length of the low-frequency resistance slope decreased after deposition and then increased after stripping. One possible explanation is that the low-frequency resistance is proportional to the Li^+ diffusion length within the SEI layer.[50,51] Thus, it is possible that the diffusion path became shorter during deposition and became longer during stripping due to the increased tortuosity.[48] However, it should be noted that the interpretation of the low-frequency resistance slope in a Nyquist plot is often controversial since the system is more complicated than a simple equivalent circuit.[52]

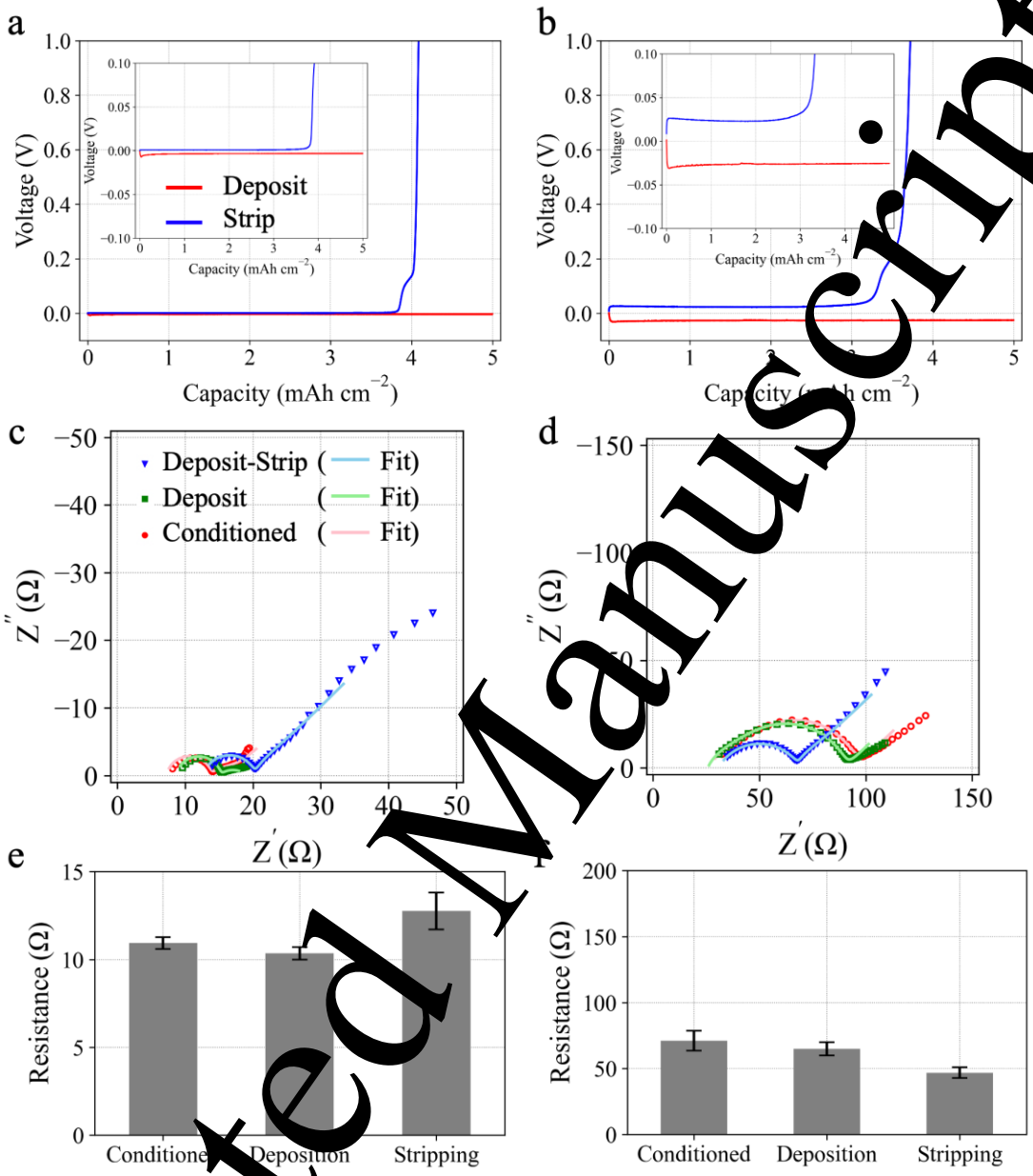

Figure 4. Voltage vs capacity curves of deep cycling of Li|PAN-ZnO cells with (a) the liquid and (b) polymer electrolytes, EIS of Li|PAN-ZnO cells with (c) the liquid and (d) polymer electrolytes. Fitted curves were added as lines. Interfacial resistance ($R_{film} + R_{ct}$) of (e) the liquid and (f) polymer electrolytes. Standard errors of the interfacial resistance are shown as error bars.

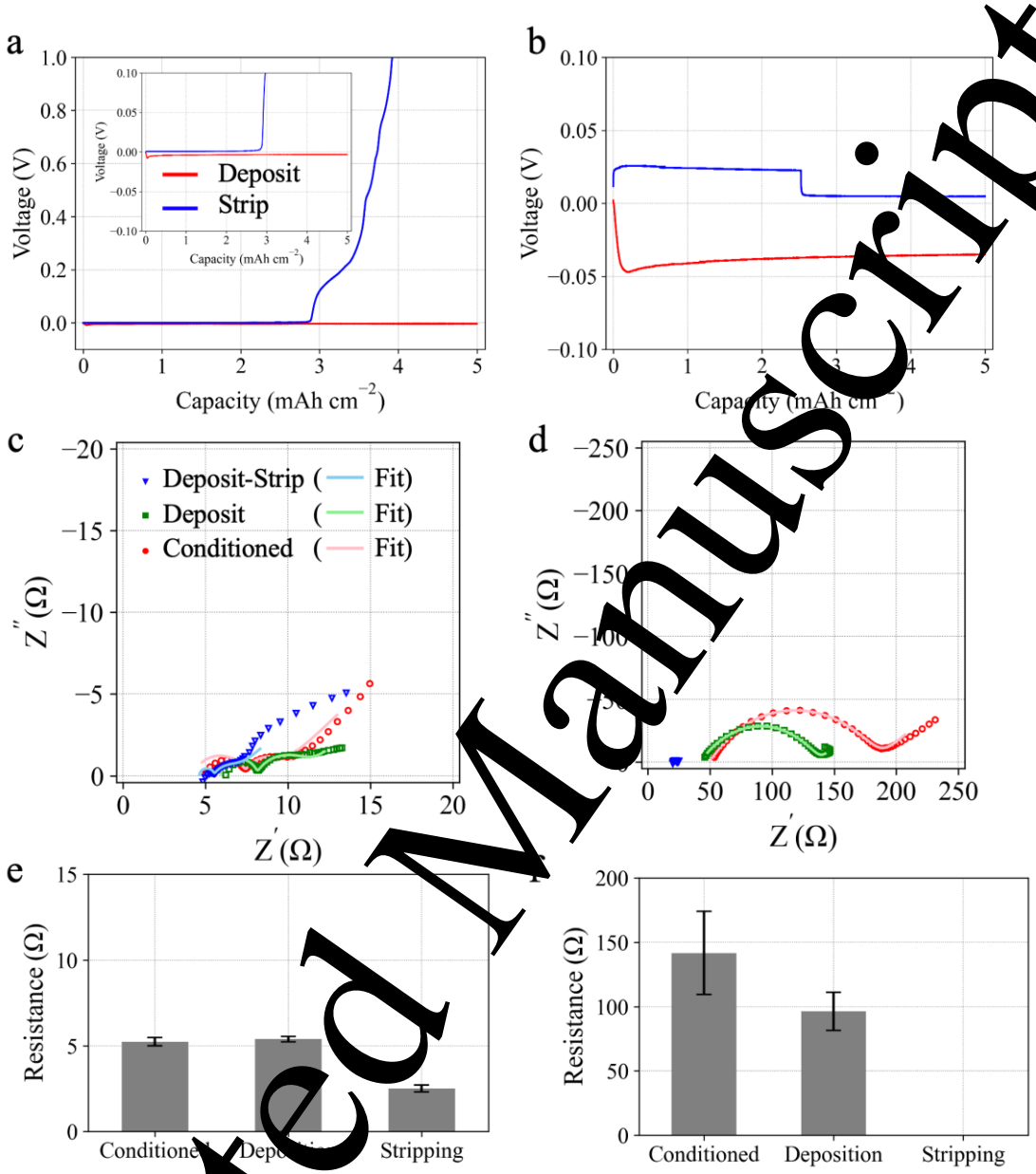

Figure 5. Voltage vs capacity curves of deep cycling of Li|Cu-ZnO cells with (a) the liquid and (b) polymer electrolytes. EIS of Li|Cu-ZnO cells with (c) the liquid and (d) polymer electrolytes. Fitted curves were added as lines. Interfacial resistance ($R_{film} + R_{ct}$) of (e) the liquid and (f) polymer electrolytes. Standard errors of the interfacial resistance are shown as error bars.

The cross-section images of both PAN-ZnO (**Figure 6**) and Cu-ZnO (**Figure 7**) electrode hosts with the polymer electrolyte were obtained via SEM at each step (before deposition, after deposition, and after stripping). The cross section of both PAN-ZnO (**Figure 6a-c**) and Cu-ZnO (**Figure 7a-c**) before deep cycling showed that the melt polymer electrolytes were homogeneously distributed and had good contact with both porous PAN-ZnO and Cu-ZnO electrodes over the entire depth (both top and bottom of the electrodes). This contact was maintained during cycling (after deposition and after stripping), showing no gap between the polymer electrolyte and the porous electrodes (**Figure 6d-i** and **Figure 7d-f**). The viscosity of the polymer electrolyte was suitable for refilling the pore volume of the PAN-ZnO and Cu-ZnO electrodes during Li deposition/stripping cycling.

The cross-section of PAN-ZnO after deposition (**Figure 6d-f**) showed that the PAN-ZnO fibers on the bottom of the matrix (**Figure 6f**) were covered with Li deposit and not visible, while the top remained unchanged (**Figure 6e**), indicating Li deposition occurred on the bottom. After stripping (**Figure 6g-i**), the top of the PAN-ZnO electrode remained unchanged (**Figure 6h**) and the bottom texture changed (**Figure 6i**), indicating that Li was stripped. However, the texture was still different from the texture of intact part (top), indicating that the bottom has Li deposit residue, which explains the low Coulombic efficiency.

The cross-section of Cu-ZnO after deposition/stripping cycling (**Figure 7**) showed the change of the texture on the top of the matrix. The bottom of the matrix appears to have a slightly different texture from before deposition, indicating that more minor Li deposition may have occurred deeper within the matrix. A previous report on a Cu-ZnO nanowire host coupled with liquid electrolyte also showed Li deposition at the top of the matrix.[34] Thus, it can be

concluded that the non-conductive PAN-ZnO electrodes was more suitable for viscous polymer electrolytes than conductive Cu-ZnO electrodes.

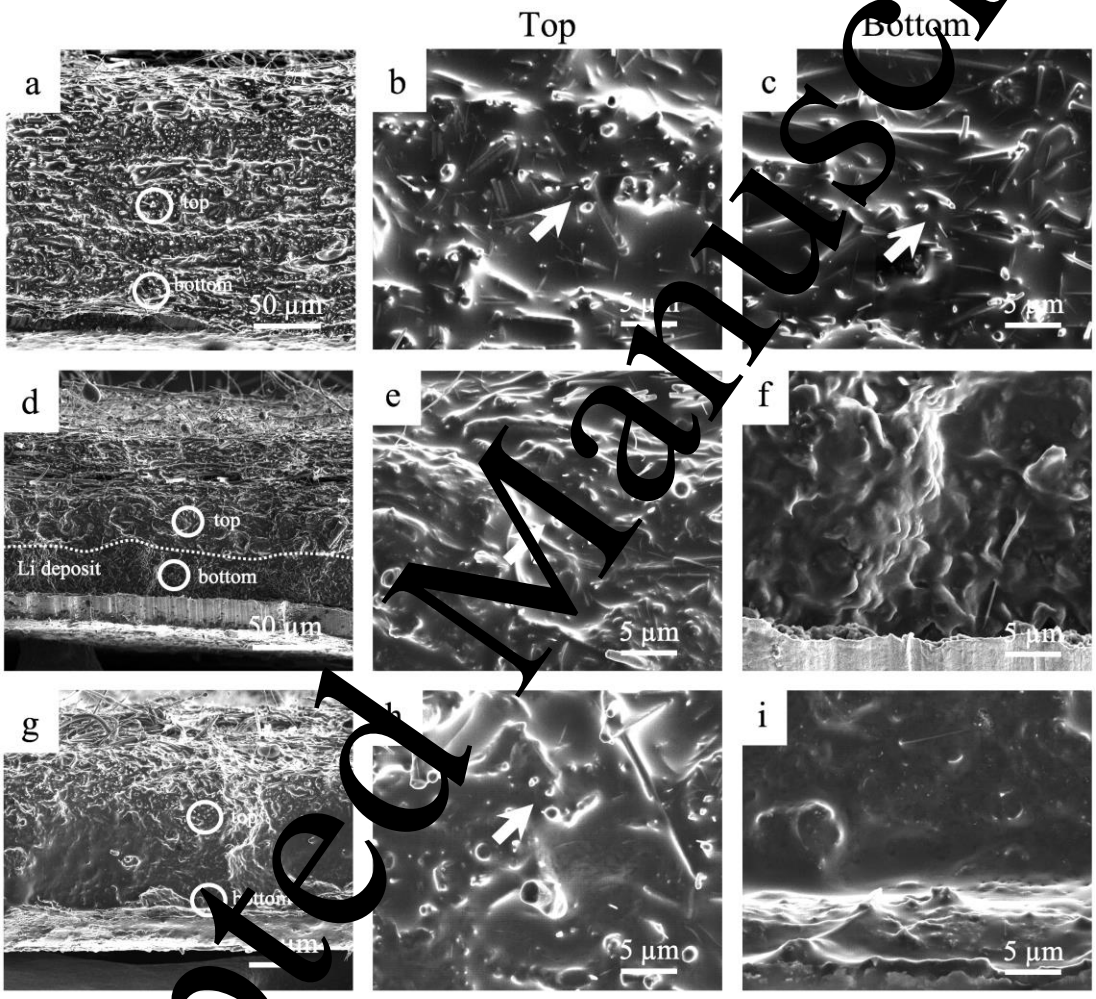

Figure 6. Cross-sectional SEM images of PAN-ZnO mat with the polymer electrolyte. (a-c) before deep deposition-stripping cycling, (d-f) after deep deposition, (g-i) after deep deposition-stripping cycling. (a, d, g) large scale, (b, e, h) small scale of top, (c, f, i) small scale of bottom. White arrows in small scale images indicate cross-section of PAN-ZnO fibers.

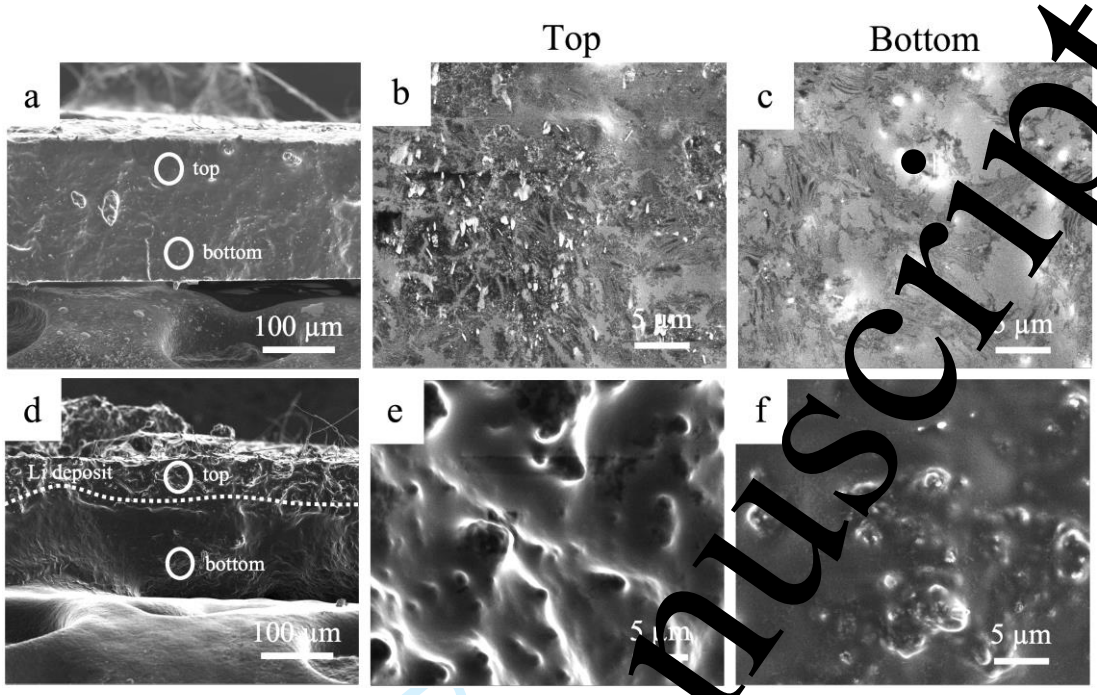

Figure 7. Cross-sectional SEM images of Cu-ZnO mat with the polymer electrolyte. (a-c) before deep deposition-stripping cycling, (d-f) after deep deposition-stripping cycling. (a, d) large scale, (b, e) small scale of top, (c, f) small scale of bottom.

3.4.Deep cycling life of Li|PAN-ZnO with the polymer electrolyte

Figure 8 compares deep cycling data with different cell types. Li|PAN-ZnO with liquid electrolyte (**Figure S8**) showed stable cycling over 15 cycles with >97% Coulombic efficiency (**Figure S9**). Li|PAN-ZnO with the polymer electrolyte was short circuited after the first successful cycle (**Figure 8b**). In comparison, Li|Cu (planar copper current collector) with the polymer electrolyte short circuited within the first deposition step (**Figure 8a**). With PAN-ZnO mats on both sides of the cell (Li+PAN-ZnO|Cu+PAN-ZnO), successful cycling was observed for 4 cycles before the cell was short circuited (**Figure 8c**). Thus, it can be concluded that the PAN-ZnO mats improved the stability of Li deposition/stripping cycling on both Cu and Li electrodes.

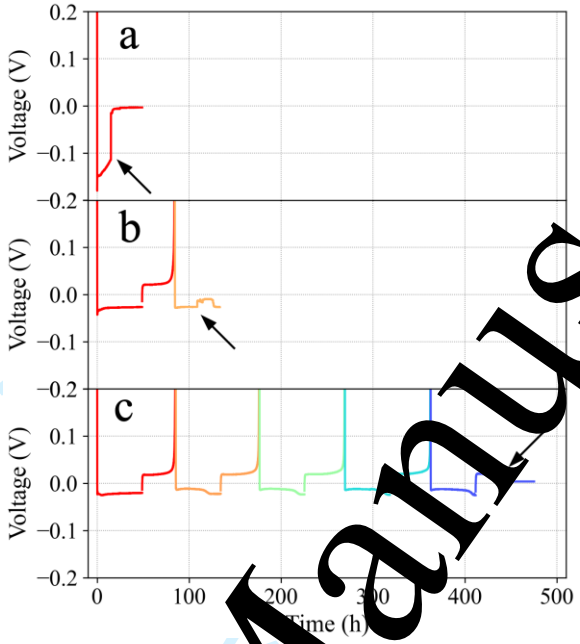

Figure 8. Deep cycling of (a) Cu|Li (without PAN-ZnO), (b) Li|PAN-ZnO (1 sheet of PAN-ZnO), and (c) Li+PAN-ZnO|Cu+PAN-ZnO (2 sheets of PAN-ZnO) with the polymer electrolyte. The arrows indicate short circuit events.

3.5.COMSOL simulation of Li deposition

COMSOL simulation results of conductive hosts and non-conductive hosts at equilibrium, where the concentration gradient and the current density did not change over time, are shown in **Figure 9** and **Figure S11**. Here, the conductive hosts and non-conductive hosts were shown as arrays of circles (cross-section of wires or fibers). Current density maps of conductive hosts with each the liquid (**Figure 9a**) and the polymer electrolyte (**Figure 9b**) showed concentrated currents on the first 2-3 layers of the substrate (rows of the arrays), mostly concentrated on the first layer. The Li^+ concentration gradient and flux maps of conductive hosts also showed that

there was no further Li^+ concentration gradient and Li^+ flux within the conductive host beyond the first two layers (**Figure 9c-d**). Non-conductive hosts (**Figure S11a-d**) showed no difference between the liquid and polymer electrolytes, showing uniform current distribution and Li^+ flux over the host volume. This explains the top deposition of Li on the conductive host in the experiments. The current density on the first layer was about 30% higher (0.13 mA cm^{-2}) than the overall current density (0.1 mA cm^{-2}) for the liquid electrolyte, while the polymer electrolyte was 100% higher (0.2 mA cm^{-2}). The electrolyte current density profiles (**Figure S12**) also show that the current density decreased more significantly from the second layer in the polymer electrolyte (maximum current of 0.15 mA cm^{-2} to 0.02 mA cm^{-2}) than the liquid electrolyte (maximum current of 0.14 mA cm^{-2} to 0.05 mA cm^{-2}), while the current density became negligible beyond the 4th layer in both electrolytes. With the liquid electrolyte in the conductive host, the electrolyte current density was 0.04 and 0.0[illegible] mA cm^{-2} on the 2nd and 3rd layers of wires, ~50% of the applied current density. On the other hand, the polymer electrolyte showed 0.01 mA cm^{-2} on the 2nd layer and became negligible from the 3rd layer, ~10% of the applied current density. Thus, Li^+ deposition might be even more focused on the top layer with the polymer electrolyte, which can result in blocking the top of the conductive host more quickly (with less capacity) and the rest of the Li deposit will eventually cause dendritic growth to short circuit the cell. In this case, the "effective area" (or "active area") for Li to be deposited was mostly limited to the first 2-3 layers. This implies that the conductive host cannot lower the local current density.

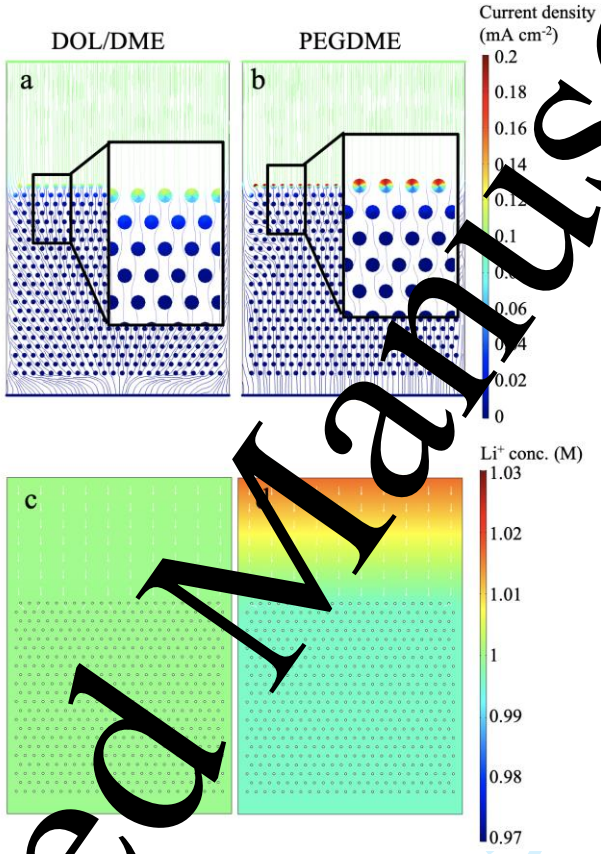

Figure 9. Current density (a, b) and Li^+ concentration (c, d) of the conductive electrode hosts via COMSOL simulations. White arrows in (c, d) indicate Li^+ flux.

4. Conclusions

Conductive and non-conductive 3D porous hosts were investigated with the viscous polymer electrolyte. It was found that the non-conductive 3D porous host was more favorable for

uniform Li deposition when the melt polymer electrolyte was employed. A first cycle of extensive Li deposition/stripping was successful with the non-conductive host maintaining good contact and refilling of the polymer electrolyte, however, the conductive host caused short circuit during this one cycle. The non-conductive host accommodated the Li deposition from the bottom, while the conductive host showed the most Li deposition on top. On the other hand, both conductive and non-conductive hosts allowed successful cycling with the liquid electrolyte during the extensive Li deposition/stripping cycling. The COMSOL simulation results indicated that the active area of the conductive host decreased and limited to the top few layers of the wires with the polymer electrolyte, which might cause blocking of the top layer more quickly. Thus, the viscous polymer electrolyte was more susceptible to block the top of the host with increased applied current density and tortuosity of conductive 3D hosts.

5. Acknowledgments

The authors gratefully acknowledge the primary financial support from the ECS Toyota Young Investigator Fellowship. Secondary financial support is also appreciated from the Creative Materials Discovery Program through the National Research Foundation of Korea funded by the Ministry of Science and ICT (2018M3D1A1057844), the Notre Dame Center for Environmental Science and Technology Predoctoral Research Fellowship (BP), National Science Foundation grant CHE1904196 and by a Berry Family Fellowship through Notre Dame's Institute for Precision Health (CO).

6. References

1. J.-M. Tarascon and M. Armand, *Nature*, **414**, 359–367 (2001).

2. S. Rothgang, M. Rogge, J. Becker, and D. U. Sauer, *Energies*, **8**, 6715–6737 (2015).

3. M. Armand and J.-M. Tarascon, *Nature*, **451**, 652–657 (2008).

4. Y. Tian, G. Zeng, A. Rutt, T. Shi, H. Kim, J. Wang, J. Koettgen, Y. Sun, B. Ouyang, T. Chen, Z. Lun, Z. Rong, K. Persson, and G. Ceder, *Chem. Rev.*, **121**, 1623–1669 (2021).

5. B. Park and J. L. Schaefer, *J. Electrochem. Soc.*, **167**, 070545 (2020).

6. B. Park, H. O. Ford, L. C. Merrill, J. Liu, L. P. Murphy, and J. L. Schaefer, *ACS Appl. Polym. Mater.*, **1**, 2907–2913 (2019).

7. B. Park, R. Andersson, S. G. Pate, J. Liu, C. P. O'Brien, G. Hernández, J. Mindemark, and J. L. Schaefer, *Energy Mater. Adv.*, **2021**, 9895203 (2021).

8. D. Aurbach, B. D. McCloskey, L. F. Nazar, and P. G. Bruce, *Nat. Energy*, **1**, 16128 (2016).

9. Q. Pang, X. Liang, C. Y. Kwok, and L. F. Nazar, *Nat. Energy*, **1**, 16132 (2016).

10. J. Liu, P. D. Pickett, B. Park, S. P. Upadhyay, S. V Orski, and J. L. Schaefer, *Polym. Chem.*, **11**, 461–471 (2020).

11. H. O. Ford, B. Park, J. Jiang, M. E. Seidler, and J. L. Schaefer, *ACS Mater. Lett.*, **2**, 272–279 (2020).

12. C. Zhang, H. Zhao, and Y. Lei, *ENERGY Environ. Mater.*, **3**, 105–120 (2020).

13. A. Eftekhari and D. W. Kim, *J. Power Sources*, **395**, 336–348 (2018).

14. K. Chayambuka, G. Mulder, D. L. Danilov, and P. H. L. Notten, *Adv. Energy Mater.*, **10**, 2001310 (2020).

15. H. D. Yoo, I. Shterenberg, Y. Gofer, G. Gershinsky, N. Pour, and D. Aurbach, *Energy Environ. Sci.*, **6**, 2265–2279 (2013).

16. R. Zhang, N.-W. Li, X.-B. Cheng, Y.-X. Yin, Q. Zhang, and Y.-G. Guo, *Adv. Sci.*, **4**, 1600445 (2017).

17. C. Fang, X. Wang, and Y. S. Meng, *Trends Chem.*, **1**, 152–158 (2019).

18. X.-B. Cheng, R. Zhang, C.-Z. Zhao, and Q. Zhang, *Chem. Rev.*, **117**, 10403–10473 (2017).

19. F. Ding, W. Xu, G. L. Graff, J. Zhang, M. L. Sushko, X. Chen, Y. Shao, M. H. Engelhard, Z. Nie, J. Xiao, X. Liu, P. V Sushko, J. Liu, and J.-G. Zhang, *J. Am. Chem. Soc.*, **135**, 4450–4456 (2013).

20. J. K. Stark, Y. Ding, and P. A. Kohl, *J. Electrochem. Soc.*, **158**, A1100 (2011).

21. X.-Q. Zhang, X. Chen, X.-B. Cheng, B.-Q. Li, X. Shen, C. Yan, J.-Q. Huang, and Q. Zhang, *Angew. Chemie Int. Ed.*, **57**, 5301–5305 (2018).

22. H. Wu, Y. Cao, L. Geng, and C. Wang, *Chem. Mater.*, **29**, 3572–3579 (2017).

23. X. Fan, L. Chen, O. Borodin, X. Ji, J. Chen, S. Hou, T. Deng, J. Zheng, C. Yang, S.-C. Liou, K. Amine, K. Xu, and C. Wang, *Nat. Nanotechnol.*, **13**, 715–722 (2018).

24. L. Ma, M. S. Kim, and L. A. Archer, *Chem. Mater.*, **29**, 4181–4189 (2017).

25. X. Liang, Q. Pang, I. R. Kochetkov, M. S. Sempere, H. Huang, X. Sun, and L. F. Nazar, *Nat. Energy*, **2**, 17119 (2017).

26. J. Lopez, A. Pei, J. Y. Oh, G.-N. Wang, Y. Cui, and Z. Bao, *J. Am. Chem. Soc.*, **140**, 11735–11744 (2018).

27. R. Bouchet, S. Maria, R. Meziane, A. Aboulaich, L. Lienafa, J.-P. Bonnet, T. N. T. Phan, D. Bertin, D. Gigmes, D. Devaux, R. Denoyel, and M. Armand, *Nat. Mater.*, **12**, 452–457 (2013).

28. H. Zhang, C. Li, M. Piszcz, E. Coya, T. Rojo, L. M. Rodriguez-Martinez, M. Armand, and Z. Zhou, *Chem. Soc. Rev.*, **46**, 797–815 (2017).

29. Q. Pang, X. Liang, A. Shyamsunder, and L. F. Nazar, *Joule*, **1**, 871–886 (2017).

30. Z. Yu, D. G. Mackanic, W. Michaels, M. Lee, A. Pei, D. Feng, Q. Zhang, Y. Tsao, C. V. Amanchukwu, X. Yan, H. Wang, S. Chen, K. Liu, J. Kang, J. Qin, Y. Cui, and Z. Bao, *Joule*, **3**, 2761–2776 (2019).

31. A. Banerjee, X. Wang, C. Fang, E. A. Wu, and Y. S. Meng, *Chem. Rev.*, **120**, 6878–6933 (2020).

32. R. Chen, Q. Li, X. Yu, L. Chen, and H. Li, *Chem. Rev.*, **120**, 6820–6877 (2020).

33. M.-H. Ryou, Y. M. Lee, Y. Lee, M. Winter, and P. Bieker, *Adv. Funct. Mater.*, **25**, 834–841 (2015).

34. L.-L. Lu, J. Ge, J.-N. Yang, S.-M. Chen, H.-B. Yao, F. Zhou, and S.-H. Yu, *Nano Lett.*, **16**, 4431–4437 (2016).

35. K.-H. Chen, A. J. Sanchez, E. Kazyak, A. L. Davis, and N. P. Dasgupta, *Adv. Energy Mater.*, **9**, 1970010 (2019).

36. C.-P. Yang, Y.-X. Yin, S.-F. Zhang, N.-W. Li, and Y.-G. Guo, *Nat. Commun.*, **6**, 8058 (2015).

37. Y. Liu, D. Lin, Z. Liang, J. Zhao, K. Yan, and Y. Cui, *Nat. Commun.*, **7**, 10992 (2016).

38. Z. Liang, D. Lin, J. Zhao, Z. Lu, Y. Liu, C. Liu, Y. Lu, H. Wang, K. Yan, X. Tao, and Y. Cui, *Proc. Natl. Acad. Sci.*, **113**, 2862–2867 (2016).

39. D. Lin, Y. Liu, Z. Liang, H.-W. Lee, J. Sun, H. Wang, K. Yan, J. Xie, and Y. Cui, *Nat. Nanotechnol.*, **11**, 626–632 (2016).

40. H. Chen, A. Pei, J. Wan, D. Lin, R. Vilá, H. Wang, D. Mackanic, H. G. Steinrück, W. Huang, Y. Li, A. Yang, J. Xie, Y. Wu, H. Wang, and Y. Cui, *Joule*, **4**, 938–952 (2020).

41. Z. Liang, G. Zheng, C. Liu, N. Liu, W. Li, K. Yan, H. Yao, P.-C. Hsu, S. Chu, and Y. Cui, *Nano Lett.*, **15**, 2910–2916 (2015).

42. X.-B. Cheng, T.-Z. Hou, R. Zhang, H.-J. Peng, C.-Z. Zhao, J.-Q. Huang, and Q. Zhang, *Adv. Mater.*, **28**, 2888–2895 (2016).

43. K. T. Peter, A. J. Johns, N. V Myung, and D. M. Cwiertny, *Water Res.*, **117**, 207–214 (2017).

44. F. Kayaci, S. Vempati, C. Ozgit-Akgun, N. Biyikli, and T. Uyar, *Appl. Catal. B Environ.*, **156–157**, 173–183 (2014).

45. A. R. Rathmell, S. M. Bergin, Y. L. Hua, Z. Y. Li, and B. J. Wiley, *Adv. Mater.*, **22**, 3558–3563 (2010).

46. X. H. Huang, X. H. Xia, Y. F. Yuan, and F. Zhou, *Electrochim. Acta*, **56**, 4960–4965 (2011).

47. J. Liu, Y. Li, X. Huang, G. Li, and Z. Li, *Adv. Funct. Mater.*, **18**, 1448–1458 (2008).

48. K.-H. Chen, K. N. Wood, E. Kazyak, W. S. LePage, A. L. Davis, A. J. Sanchez, and N. P. Dasgupta, *J. Mater. Chem. A*, **5**, 11671–11681 (2017).

49. B. Wu, J. Lochala, T. Taverne, and J. Xiao, *Nano Energy*, **40**, 34–41 (2017).

50. P. Biswal, S. Stalin, A. Kludze, S. Choudhury, and L. A. Archer, *Nano Lett.*, **19**, 8191–8200 (2019).

51. F. Single, B. Horstmann, and A. Latz, *J. Phys. Chem. C*, **123**, 27327–27343 (2019).

52. J. Huang, *Electrochim. Acta*, **281**, 170–188 (2018).

Supporting Information

Title

Coupling of 3D Porous Hosts for Li Metal Battery Anodes with Viscous Polymer Electrolytes

Authors

Bumjun Park,[1] Christiana Oh,[1] Sooyoun Yu,[1] Bingxin Yang,[1] Nosang V. Myung,[1] Paul W. Bohn,[1,2] Jennifer L. Schaefer[1,z]

[1] Department of Chemical and Biomolecular Engineering, University of Notre Dame, Notre Dame, Indiana 46556, United States

[2] Department of Chemistry and Biochemistry, University of Notre Dame, Notre Dame, Indiana 46556, United States

[z][Jennifer.L.Schaefer.43@nd.edu]

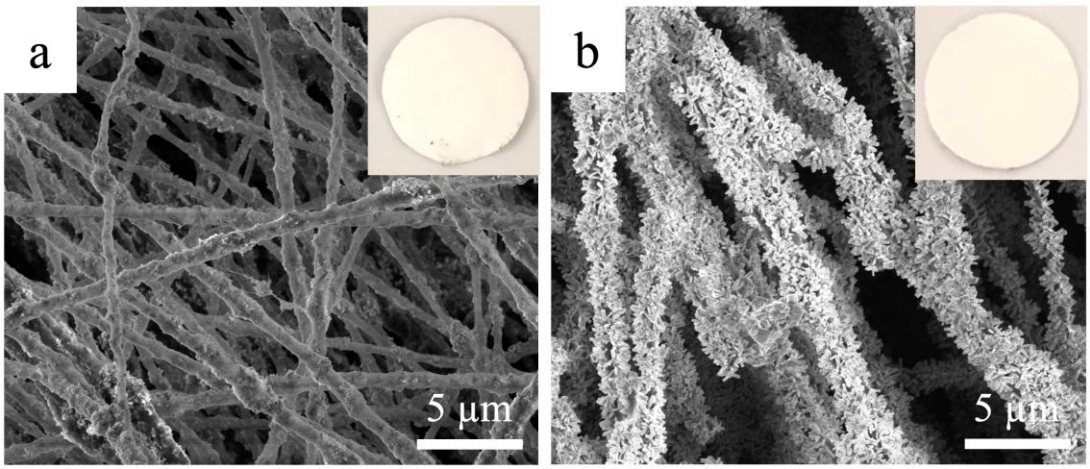

Figure S1. SEM images of PAN-ZnO mat before thermal stabilization: (a) as electrospun, (b) after hydrothermal growth.

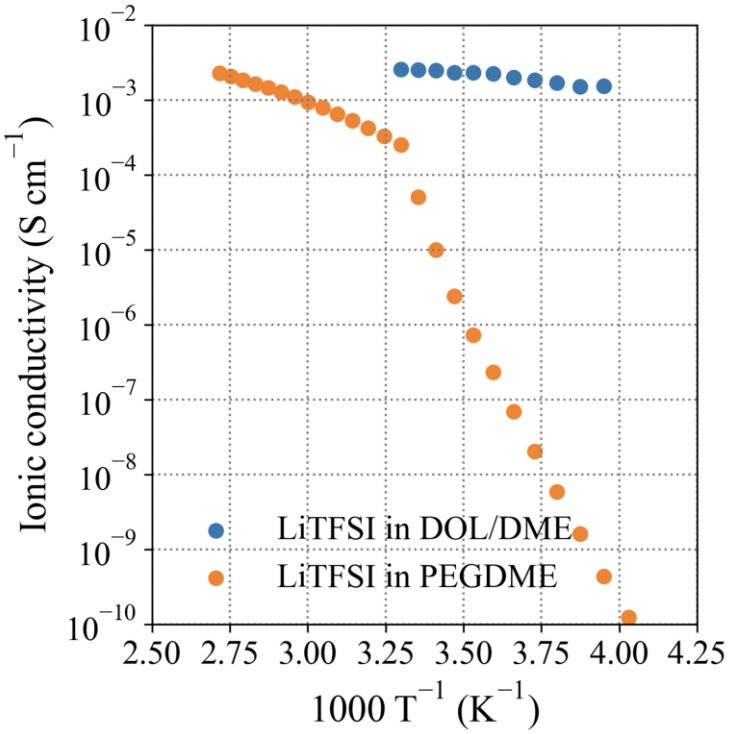

Figure S2. Ionic conductivity vs inverse temperature (1000 T^{-1}) of LiTFSI in DOL/DME and LiTFSI in PEGDME (M_n = 1000 (g mol^{-1})).

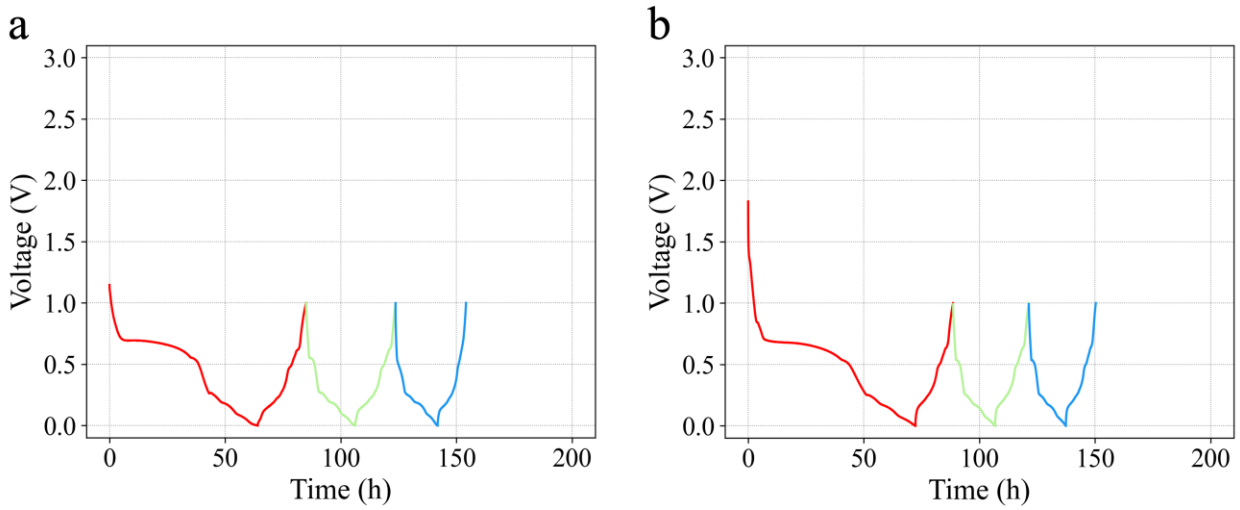

Figure S3. Voltage vs time curves of the conditioning step of Li|PAN-ZnO cells with (a) the liquid and (b) polymer electrolytes.

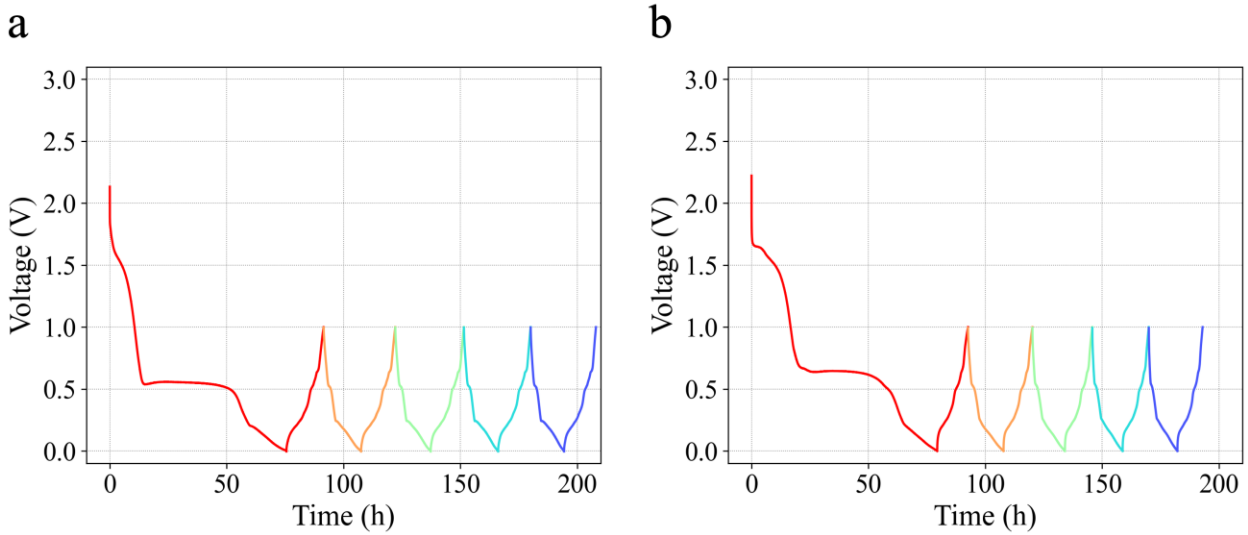

Figure S4. Voltage vs time curves of the conditioning step of Li|Cu-ZnO cells with (a) the liquid and (b) polymer electrolytes.

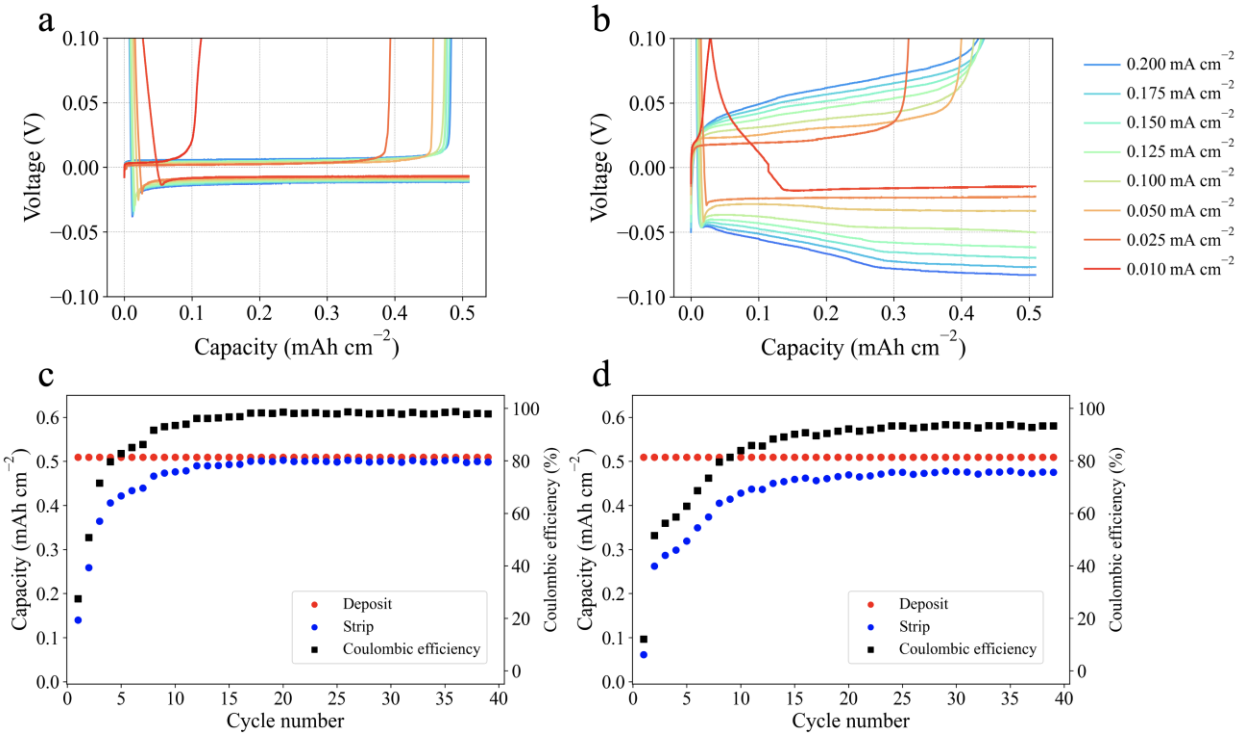

Figure S5. Rate capability of Li|PAN-ZnO cells at different current rates (0.01 – 0.2 mA cm^{-2}). Voltage vs capacity curves at each rate with (a) the liquid and (b) polymer electrolytes. Charge and discharge capacity and Coulombic efficiency vs cycle number with (c) the liquid and (d) polymer electrolytes.

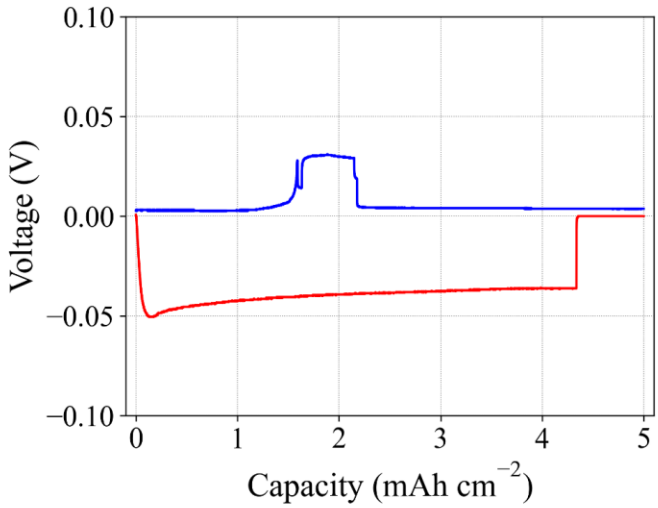

Figure S6. Voltage vs capacity curve of Li|Cu-ZnO with the polymer electrolyte in a deep cycling step. The cell was short circuited at the end of deposition.

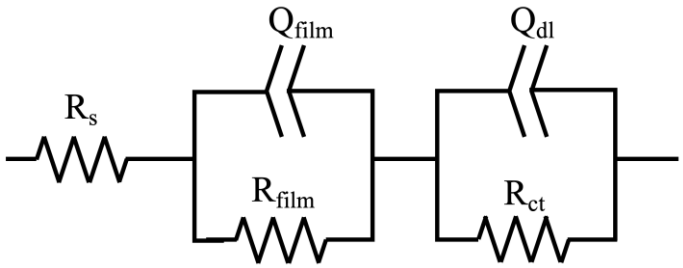

Figure S7. The equivalent circuit used to fit the EIS data.

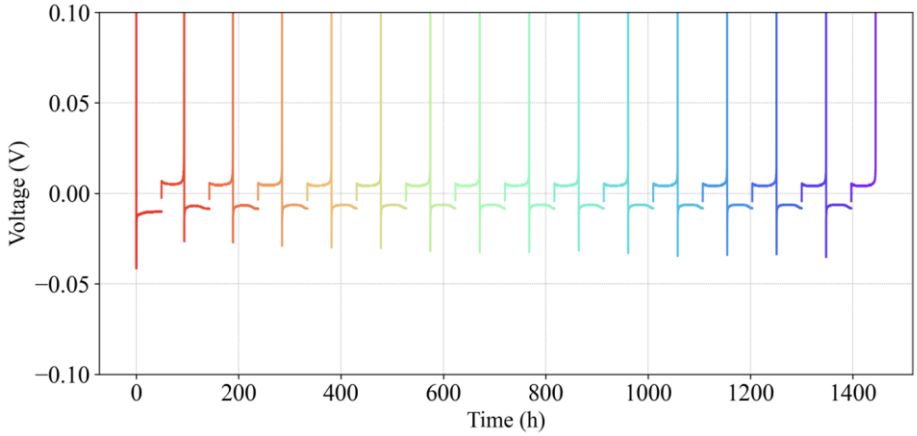

Figure S8. Deep cycling of Li|PAN-ZnO with the liquid electrolyte

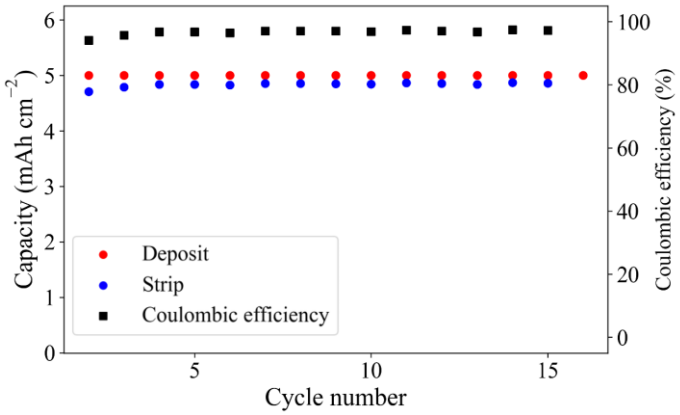

Figure S9. Deep cycling capacity and coulombic efficiency over cycles with Li|PAN-ZnO cell with the liquid electrolyte.

COMSOL Simulations (Cu Nanowires): Finite element simulations were performed using COMSOL Multiphysics v5.4 using the Electrochemistry Module. A 2-dimensional geometry was developed to represent the electrolyte domain over a 100 µm × 160 µm area (in grey), as shown in **Figure S10**. No volume changes were associated with the electrodes and the electrolyte domain area was kept constant.

In these simulations, all domain equations are derived from the Nernst-Planck Equation, given by:

$$\frac{\partial c_i}{\partial t} + \nabla \cdot (\boldsymbol{J}_i + c_i \boldsymbol{u}) = R_{i,tot}$$

where c_i denotes the concentration of species i (mol m^{-3}), $\boldsymbol{u}$ is the velocity vector (m s^{-1}), and $\boldsymbol{J}_i$ is the molar flux relative to the convective transport. Here, the total flux of all species $\boldsymbol{N}_i$ (mol m^{-2} s^{-1}) considers the flux of all charged species by diffusion, migration, and convection:

$$\boldsymbol{N}_i = (\boldsymbol{J}_i + c_i \boldsymbol{u}) = -D_i \nabla c_i - z_i u_{m,i} F c_i \nabla \phi_l + c_i \boldsymbol{u}$$

where c_i is the concentration of species i (mol m^{-3}), z_i is the valence, D_i is the diffusion coefficient (m^2 s^{-1}), $u_{m,i}$ is the mobility, F is Faraday's constant (C mol^{-1}), ϕ_l is the electrolyte potential.

The simulations consider one species of interest, Li^+ ion, where the electrode reactions were governed by the following process:

$$Li^+ + e^- \leftrightarrow Li\ (s)$$

Here, the Li metal anode is designated as the top boundary of the electrolyte domain where Li ion generation by dissolution occurs, while the Cu electrodes is designated as the bottom boundary where Li depletion by Li metal deposition occurs. Therefore, the exact dimensions of the Li metal anode and Cu electrodes are not considered since the electrochemical reactions only take place at the electrode/electrolyte interfaces and the conductivities for both

electrodes are very high. Here, the reaction kinetics associated with Li^+ ion generation on the Li metal and depletion on the Cu nanowires and Cu electrode surfaces were described by a Butler-Volmer expression for the charge transfer current density i_{loc} (A m^{-2}), given by:

$$i_{loc} = i_o \left(\exp\left(\frac{\alpha_a F \eta}{RT}\right) - \exp\left(\frac{-\alpha_c F \eta}{RT}\right) \right)$$

where α_a is the anodic charge transfer coefficient, α_c is the cathodic transfer coefficient, and η is the overpotential. The exchange current density i_o (A m^{-2}) is related to the heterogeneous rate constant k_o (m s^{-1}) expressed as:

$$i_o = k_o F c$$

The stoichiometric notations used in the physics interfaces follow a general electrochemical reaction expression:

$$\sum_{ox} v_{ox} S_{ox} + ne^- \leftrightarrow \sum_{red} v_{red} S_{red}$$

where the stoichiometric coefficients, v_i, are positive (v_{ox}) for products and negative (v_{red}) for reactants in a reduction reaction.

To study the effects of nanowire electrode tortuosity and conductivity on Li ion transport and current density distribution in the cell, a 100 µm × 100 µm domain of circular nanowires (d = 1µm, porosity 85%) was incorporated into the electrolyte structure. This domain is located 50 µm below the top Li anode boundary to simulate a bulk electrolyte layer above the nanowires. Simulations were undertaken for both Cu nanowires and PAN-ZnO nanowires. For simulations with Cu nanowires, identical electrode boundary conditions were designated for Cu nanowires and the bottom Cu electrode where the total current was set to 0.1 mA. The domain equation for the electrode boundaries is given by:

$$\nabla \cdot i_s = Q_s$$

where, the current density vector i_s is given by:

$$i_s = -\sigma_s \nabla \phi_s$$

and Q_s is the current source (A m^{-3}), σ_s is the electrode's conductivity, and ϕ_s is the electric potential.

To study the effects of electrolyte materials (PEGDME, DOL/DME) in the simulations, properties such as the diffusion coefficient of Li^+, electrolyte conductivity, transport number, and activity coefficient were considered. These are summarized for PEGDME and DOL/DME in **Table S1**. Electrolyte salt concentrations were designated as 1×10^3 mol m^{-3} for both electrolytes.

Table S1. Designated Material Properties for Electrolytes (PEGDME, DOL/DME).

	PEGDME	**DOL/DME**
Diffusion coefficient (m^2 s^{-1})	2.0×10^{-11}	5.0×10^{-10}
Electrolyte conductivity (S m^{-1})	6.50×10^{-2}	2.92×10^{-1}
Transport number	0.30	0.50

Here, the domain equation for the current balance in the electrolyte is expressed as:

$$\nabla \cdot \boldsymbol{i_l} = 0$$

And the expression for the current density vector in the electrolyte, $\boldsymbol{i_l}$ (A m^{-2}), is given by:

$$i_l = F \sum z_i \boldsymbol{N_i}$$

where the net current density can be described as the sum of all species fluxes. From the Nernst-Planck equation, we can derive the following expression for the total flux $\boldsymbol{N_i}$ by substituting the Nernst-Einstein relation for the electrical mobility of an ion:

$$\boldsymbol{N}_i = -D_i\left(\nabla c_i + \frac{z_i F}{RT} + c_i \nabla \phi_l\right) + c_i \boldsymbol{u}$$

Thus we obtain:

$$i_l = -F\sum D_i z_i \nabla c_i - \frac{F^2}{RT}\nabla\phi_l \sum {z_i}^2 D_i c_i + \boldsymbol{u}\sum z_i\, c_i$$

which can be further simplified by eliminating the diffusion current and convection terms to:

$$i_l = -\sigma_l \nabla \phi_l$$

which is defined by the following expression for the electrolyte conductivity (σ_l):

$$\sigma_l = F^2 \sum {z_i}^2\, u_{m,i} c_i$$

For all simulations, time-dependent solutions were obtained over a total range of 2000 s to ensure that steady state solutions were reached (where concentrations and current did not change over 10s of seconds). Specifically, solutions were obtained over 4 distinct time ranges: the first range of solutions were obtained from t = 0 s to 1 s at 0.1 s intervals to determine Li^+ ion transport at early stages of charging. The next set of solutions was obtained from t = 2 s to 10 s at 1 s intervals, followed by another set of solutions obtained from t = 20 s to 100 s at 10 s intervals. Finally, the last set of solutions was obtained from t = 200 s to 2000 s at 100 s intervals to study longer term Li transport phenomena. The figures in the text were taken at t = 2000 seconds and 200 seconds of the simulations for PEGDME and DOL/DME, respectively. For simulations with PEGDME, steady state is reached at t = 900 seconds, while simulations with DOL/DME reach steady state at t = 50 seconds.

COMSOL Simulations (PAN-ZnO):

COMSOL simulation results for model systems using PAN-ZnO nanowires are shown in **Figure S11**. Here, the simulations undertaken were identical to the ones described above, with

the exception that the circular nanowires were designated as insulating boundaries instead. Thus, no Li depletion by deposition was simulated on PAN-ZnO nanowire surfaces. Electrolyte effects on Li transport and current density distribution were also investigated by varying the electrolyte (PEGMDE, DOL/DME) for these simulations. The figures in the **Figure S11** were taken at t = 2000 seconds and 200 seconds of the simulations for PEGDME and DOL/DME, respectively. For simulations with PEGDME, steady state is reached at t = 600 seconds, while simulations with DOL/DME reach steady state at t = 50 seconds.

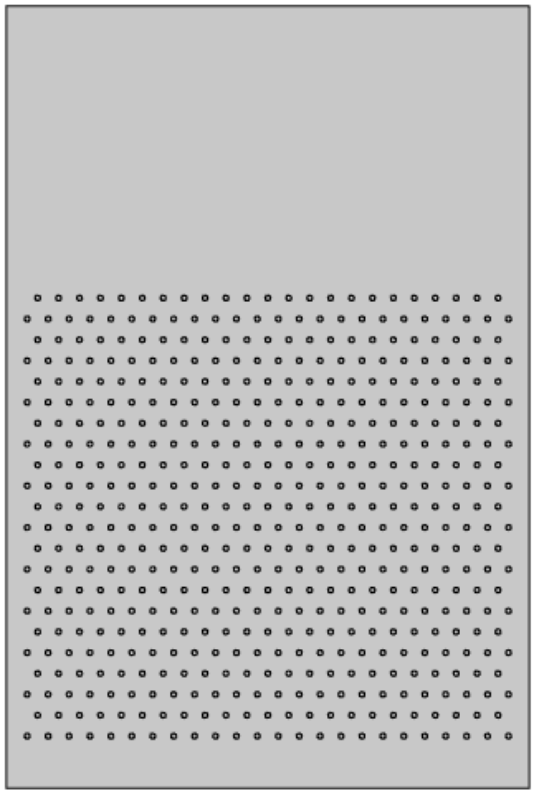

Figure S10. Simulation cell geometry (100 μm × 160 μm) in COMSOL.

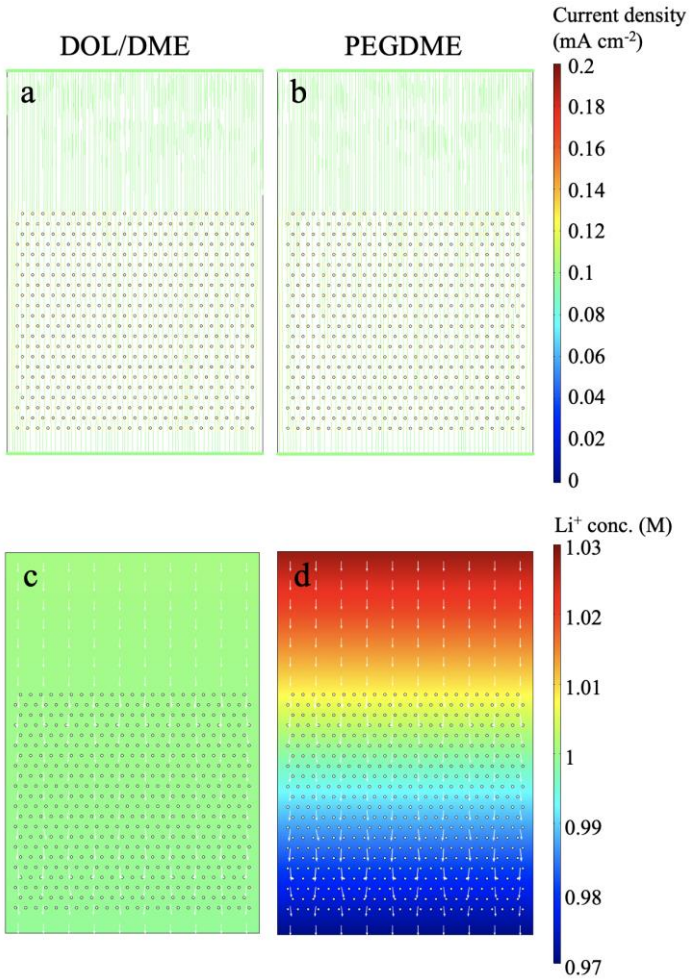

Figure S11. Current density (a, b) and Li^+ concentration (c, d) of the non-conductive electrode hosts via COMSOL simulations. White arrows in (c, d) indicate Li^+ flux.

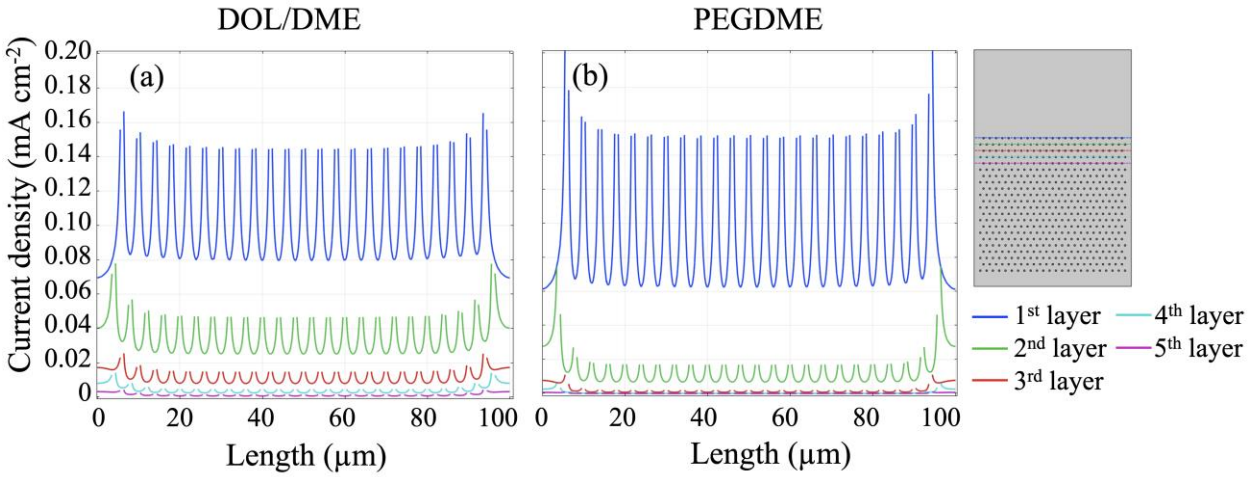

Figure S12. Electrolyte current density profiles on the lines on the first five layers of the conductive substrate in (a) the liquid and (b) polymer electrolytes. X-axis indicates the distance from the left side.